Nardelli et al. *EPJ Quantum Technology* (2020) 7:11
https://doi.org/10.1140/epjqt/s40507-020-00086-4

EPJ Quantum Technology
a SpringerOpen Journal

RESEARCH Open Access

# A conformal array of microfabricated optically-pumped first-order gradiometers for magnetoencephalography

N.V. Nardelli[1], A.R. Perry[1], S.P. Krzyzewski[1] and S.A. Knappe[1,2*]

*Correspondence:
svenja.knappe@colorado.edu
[1]University of Colorado Boulder, Boulder, CO 80309, USA
[2]FieldLine Inc., Boulder, CO 80301, USA

**Abstract**

An array of 21 first-order gradiometers based on zero-field optically-pumped magnetometers is demonstrated for use in magnetoencephalography. Sensors are oriented radially with respect to the head and housed in a helmet with moveable holders which conform to the shape of a scalp. Our axial gradiometers have a baseline of 2 cm and reject laser and vibrational noise as well as common-mode environmental magnetic noise. The median sensitivity of the array is 15.4 fT/Hz$^{1/2}$, measured in a human-sized magnetic shield. All magnetometers are operated independently with negative feedback to maintain atoms at zero magnetic field. This yields higher signal linearity and operating range than open-loop operation and a measurement system that is less sensitive to systematic and ambient magnetic fields. All of the system electronics and lasers are compacted into one equipment rack which offers a favorable outlook for use in clinical settings.

**Keywords:** Magnetometer; Atomic; Laser sensors; Quantum sensors; Optical instruments; Micro-optical devices; Spin-exchange relaxation-free (SERF); Magnetoencephalography (MEG); Optically-pumped magnetometer (OPM)

## 1 Introduction

Measuring DC magnetic fields with high precision is important for biomedical imaging applications such as magnetoencephalography (MEG) [1]. Neuronal signals inside the brain create small magnetic fields that penetrate the skull largely undisturbed and these fields can be detected by an array of sensitive magnetometers placed centimeters to millimeters from the surface of the scalp. Reconstruction algorithms can use the combined magnetometer data to create 3D current density maps with high spatial and timing resolution [2, 3].

Superconducting Quantum Interference Devices (SQUIDs) have become the predominant tool for MEG applications [4, 5], where roughly 300 low-temperature SQUID sensors are placed into a head-shaped liquid helium dewar. Over the last 10 years, optically-pumped magnetometers (OPMs), relying on alkali atoms in vapor cells, have emerged as one possible alternative. The non-cryogenic nature is one attractive feature of OPMs, which not only eliminates the need for frequent replenishing of helium, but also allows for

conformal placement of the sensors within millimeters of the scalp, independent of head size and shape. A series of simulation studies predicted clear improvements in signal-to-noise ratio of OPMs compared to SQUIDs due to the closer proximity, despite the higher noise floor of OPMs [6–9].

Zero-field OPMs are of special interest to MEG due to their low noise floor when operating in the Spin-Exchange Relaxation-Free (SERF) regime [10, 11]. When the rate of atomic spin-exchange collisions exceeds the Larmor precession rate, the atomic decoherence due to spin exchange is eliminated, resulting in a narrow atomic resonance. Operating in this regime requires low ambient DC magnetic fields, lending itself to the MEG application, where high-quality images necessitate a high degree of magnetic shielding to reject environmental noise. Currently, SQUID systems require magnetically-shielded rooms (MSRs) to house large dewar systems while OPM arrays can be contained inside of small cylindrical shields that are more cost-effective and provide a higher degree of ambient field rejection than MSRs.

Building off of previous designs [12–15], we demonstrate a multichannel OPM system capable of synchronously operating 48 microfabricated SERF magnetometers in an array of 24 radial first-order gradiometers. Several MEG recordings have been published to date with conformal OPM arrays with more than 10 channels [13, 16–19]. While most OPM arrays consist of magnetometers, a system of planar gradiometers, measuring both transverse components of the magnetic field, has been developed by the Sandia group [16, 17, 20]. In contrast, the gradiometers in this work measure the radial component and radial gradient with a 2 cm baseline and can be adjusted such that their position conforms to the shape of a human head. To our knowledge, this is the first demonstration of this kind in an array configuration with OPMs.

Our gradiometer layout allows the suppression of noise induced by the laser and optical fibers, as well as common-mode environmental magnetic noise. In addition, we operate each magnetometer in closed-loop mode whereby the open-loop magnetometer output is fed back onto a Helmholtz coil pair to keep the alkali atoms at zero field [21]. This provides a number of performance enhancements over open-loop OPM systems, including increased common-mode rejection ratios of the gradiometers [12], higher signal linearity and robustness to magnetic drift, and an increased dynamic range.

## 2 Methods

### 2.1 Gradiometer design

Our magnetic gradiometer design contains two microfabricated $^{87}$Rb vapor cells, separated center-to-center by 2 cm [12]. The distance between the tip of each sensor and the center of the cell closest to the scalp is roughly 4 mm.

A single 795 nm (1-2 mW) laser beam, delivered to the sensor via a polarization-maintaining fiber, is linearly polarized and collimated to 2 mm before being split by a 50/50 beam splitter and sent through two $^{87}$Rb vapor cells. Each beam is circularly polarized with a quarter-wave plate before the vapor cell to polarize the $^{87}$Rb atomic spins. The light transmitted through each cell contains magnetic field information as seen by the alkali atoms and is detected by a photodiode. Two single-mode fibers deliver 1540 nm light to each cell, which heat the $^{87}$Rb vapor cells to approximately 150°C.

Each vapor cell has an inner volume of $3 \times 3 \times 2$ mm$^3$ and is made from a silicon rim anodically bonded to borosilicate glass windows on the front and back. A color filter is

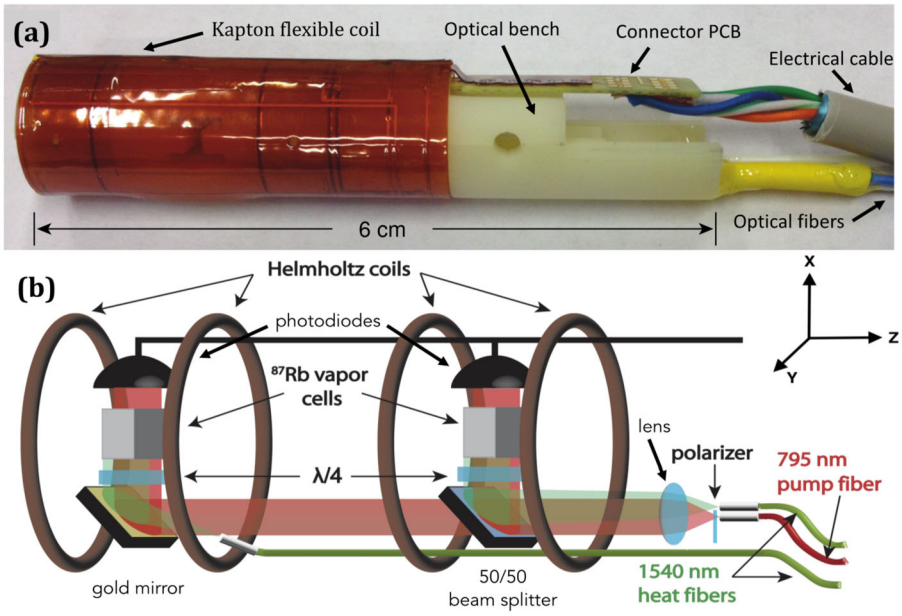


**Figure 1** (**a**) Photograph of the magnetic gradiometer. (**b**) Plot of laser paths inside sensor. The pump/probe laser/fiber is shown in red and heat laser/fiber is shown in green. $^{87}$Rb cells are separated by a baseline of 2 cm

glued to the outside of each window to absorb the 1540 nm light for vapor cell heating [22] while passing the pump/probe light at 795 nm. Each cell contains a droplet of $^{87}$Rb and about 1 amg of $N_2$ to act as a buffer gas and to prevent radiation trapping. The vapor cell is embedded in a microfabricated vacuum package, suspended on a web of polyimide to minimize conductive heat losses [23] and to prevent subject discomfort due to excess heat, while maintaining a short standoff distance of 4 mm. Each cell requires 150–200 mW of 1540 nm light to maintain an optimal vapor density.

A flexible PCB wrapped around each sensor contains traces for four magnetic field coils: one Helmholtz pair along the sensor axis for each cell to control field offsets and to provide lock-in modulation fields in the measurement direction ($z$ direction in Fig. 1(b)) and two saddle coils to provide a common field offset to both cells in the transverse directions ($x$ and $y$ directions in Fig. 1(b)).

## 2.2 Gradiometer array design

An 80 mW diode laser [24] delivers light at 795 nm through a 1 × 24 polarization-maintaining (PM) fiber splitter to a maximum of 24 gradiometers and is responsible for pumping/probing the $^{87}$Rb D1 line. Forty-eight pigtailed 1540 nm laser diodes, necessary to heat the 48 $^{87}$Rb cells through absorption by colored glass glued to each cell [15], are mounted on PCBs designed to fit in a 19-inch rack (Fig. 2(a)). The output power of each laser diode is controlled independently by a feedback loop to keep the temperature of each cell constant. This is achieved by monitoring the 795 nm DC power that is transmitted through the vapor cell which can be controlled by changing the absorption of the $^{87}$Rb vapor by adjusting the 1540 nm power. Due to the good thermal isolation of the cell inside the vacuum package, thermal time constants are around 10 seconds. This eliminates concern for temperature drifts in the lab and kinks in the heat fiber.

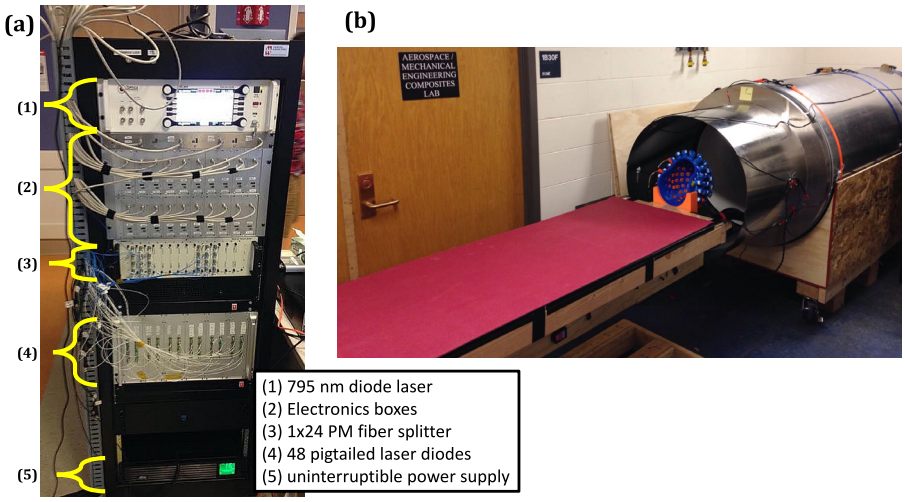


**Figure 2** (**a**) MEG electronics rack: the 1 × 24 PM fiber splitter splits laser output for pump/probe and 48 pigtailed laser diodes provide light for vapor cell heating. An uninterruptible power supply provides power to entire rack. (**b**) Human-sized magnetic shield and bed setup with mounted 3D-printed helmet for holding OPMs

Twenty-four electronics control boards [25] generate and receive signals for each sensor, as well as process the magnetometer signals. Sinusoidal magnetic modulation fields at 1.77 kHz are applied to each magnetometer via Helmholtz coils for lock-in detection. The electronics boards also send DC current to Helmholtz and saddle coils to control the individual offset fields (in three directions) on each sensor. Each board also receives two magnetometer photodiode signals which are amplified and mixed in digital lock-in amplifiers to generate the open-loop magnetometer outputs. These outputs are then fed back to adjust the current to the Helmholtz coils, which locks the magnetometer signals to the zero-crossing of the magnetic resonance. These feedback current signals are direct representations of the fields seen by the atoms and are operated independently for both cells in each gradiometer. Signals are recorded with an array of 24-bit DAQs at a sample rate of 5 kS/s. The 1.77 kHz modulation of all sensors is synchronized to a master signal to avoid beat signals in the data.

The two heat fibers, a PM fiber, and a shielded cable with electrical inputs and outputs extend 6 m so sensor heads and the control electronics can be spatially separated to allow telemetric measurements with minimal magnetic interference from the rack.

## 3 Results and discussion

### 3.1 System performance

Gradiometers suppress correlated noise, including laser frequency and intensity noise, fiber polarization noise, and common-mode magnetic noise. The pump/probe light is delivered to each sensor via a polarization-maintaining fiber, which picks up a large amount of mechanical noise due to fiber movement. Some of the mode-competition noise can be suppressed by modulating the laser frequency at 1 MHz, which helps to average out the index changes due to mechanical fluctuations. We have previously shown that the common-mode rejection ratio of the gradiometers increased from 70 to 500–1000, by operating under negative feedback [12]. This is due to much lower drifts of the magnetic

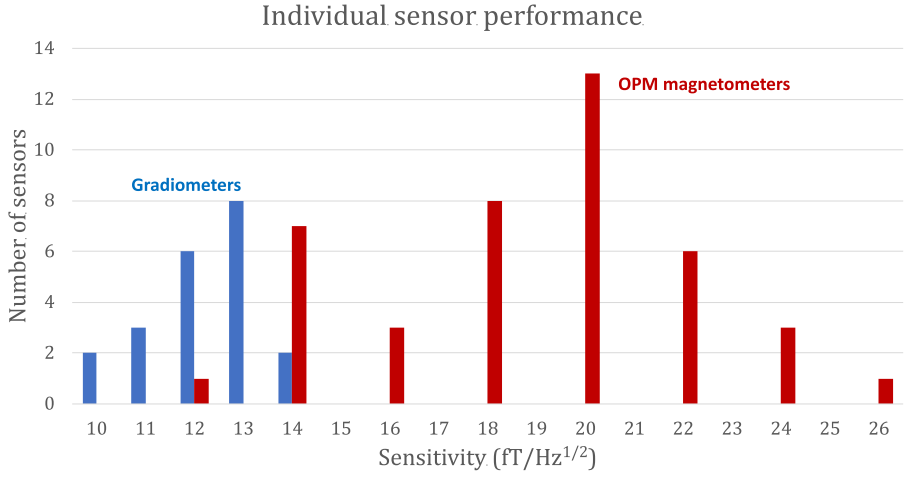


**Figure 3** Sensor performance when measured individually inside a magnetically well-shielded environment with good vibration isolation

calibration factors of each of the two magnetometer arms. Open-loop scale factors depend on laser and cell parameters as well as the magnetic field environment, while closed-loop scale factors largely depend on the coil geometry only.

First, the noise floors of all magnetometers and gradiometers were individually measured inside a table-top magnetic shield. Figure 3 shows a histogram of sensor sensitivity values, measured as the average magnetic field equivalent noise between 10–50 Hz for magnetometers (red) and gradiometers (blue). For easier direct comparison with the magnetometer, we are showing gradiometer noise in units of $\mathrm{fT/Hz^{1/2}}$ (gradiometer noise in $\mathrm{fT/cm/Hz^{1/2}} \times 2$ cm baseline). A synthetic gradiometer built out of two magnetometers, each having an uncorrelated noise floor of 10 $\mathrm{fT/Hz^{1/2}}$ in a noiseless homogenous field is expected to have a gradiometer noise of $\sqrt{2} \times 10\ \mathrm{fT/Hz^{1/2}}$, independent of the baseline, since the noise of the two magnetometers adds in quadrature.

Nevertheless, it can be seen from Fig. 3 that the OPM gradiometers perform better than the OPM magnetometers. This is largely due to additional noise on the light of the pump/probe fiber, which is suppressed by the gradiometers. It can also be seen that the gradiometers all have noise floors of $7\ \mathrm{fT/cm/Hz^{1/2}} \times 2\ \mathrm{cm} = 14\ \mathrm{fT/Hz^{1/2}}$ of lower, some as low as $10\ \mathrm{fT/Hz^{1/2}}$. This implies that the individual magnetometers support a sensitivity of $7\ \mathrm{fT/Hz^{1/2}}$ (since the noise of both magnetometers add in quadrature) in a small sensitive volume of $3 \times 3 \times 2\ \mathrm{mm^3}$, which is consistent with our previous results [26].

After individual testing, the gradiometers were assembled into an array driven by one common pump/probe laser. The system was placed onto a helmet-shaped holder inside a human-sized cylindrical shield can consisting of 2 layers of mu-metal, of diameters 86 cm and 97 cm respectively, and 2 layers of aluminum (shown in Fig. 2). Figure 4 shows the simultaneous averaged sensitivity of 42 magnetometers in comparison with 21 gradiometers. Note that the system is capable of supporting 24 gradiometers (48 magnetometers) but we only had 21 pairs of OPMs available at the time of this measurement. This is due mainly to the fact that our first iteration of vacuum-packaged cells resulted in some cells whose vacuum seal degraded such that the light from the 1540 nm diodes was not sufficient to heat the vapor into the SERF regime.

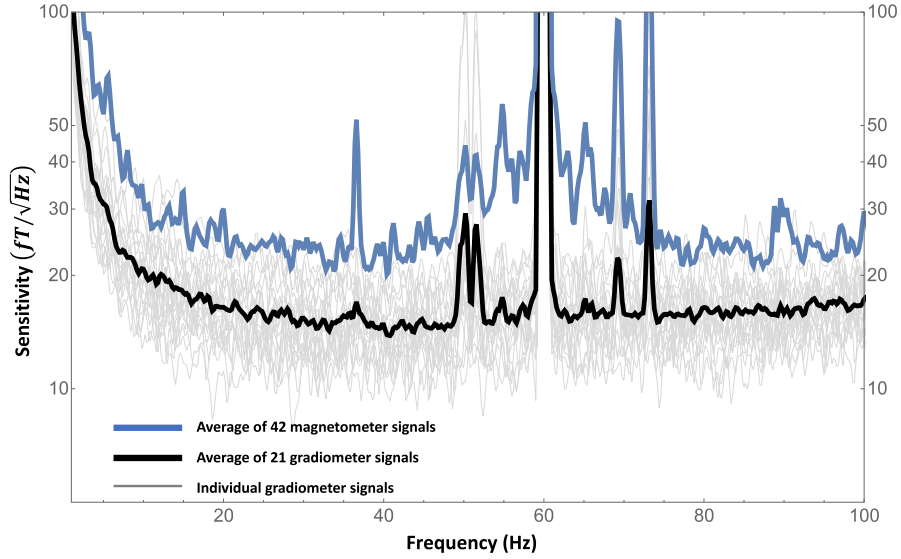


**Figure 4** Magnetic noise baseline for 21 gradiometers and their constituent magnetometers in a human-sized shield

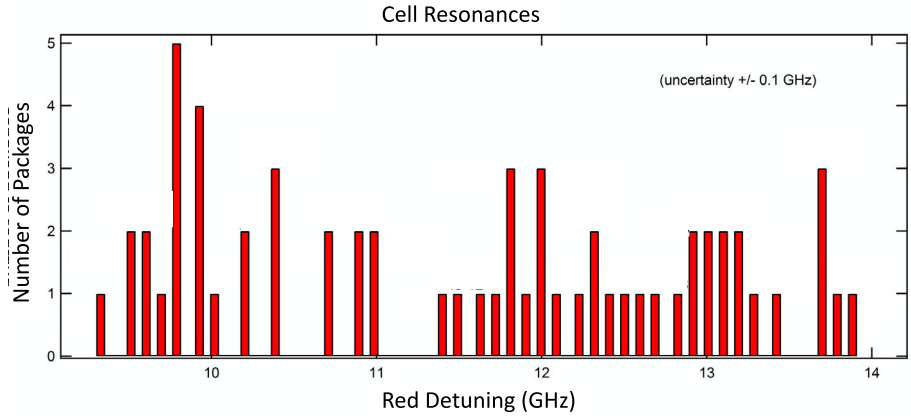


**Figure 5** Histogram of number of cells as a function of detuning of the resonance frequency of the cells with respect to a pure Rb cell

The gradiometer sensitivity ranged from 10–24 fT/Hz$^{1/2}$, with a median of 15.4 fT/Hz$^{1/2}$, averaged from 10–50 Hz in the human-sized shield. Evoked responses typically have signal strengths of several hundred fT and up to several pT at the scalp, which are not only well above the noise floor of our system but are also detectable by sensors several cm away from the source. The gradiometer signals remain relatively flat, excluding a large vibrational noise peak between 40–80 Hz that the magnetometers exhibit. The system is located in a very mechanically and magnetically noisy environment and the shield is only slightly passively vibration-isolated from the ground.

The degradation of the array performance as compared to that of the individual gradiometers was caused by the use of one common pump/probe laser. Variations in the nitrogen buffer gas pressure of each cell led to a slightly different atomic resonance frequency spanning 10 GHz, as can be seen in Fig. 5. The cells were paired into gradiometers

with similar pressures to match the FM-AM noise conversion of the two cells to reduce this noise source. The pump/probe light was tuned to an average frequency of 377.095 THz. This sacrificed about 10% sensitivity for those cells where the pump/probe laser and resonant frequency were mismatched.

The setup was complicated by an unequal pump/probe power split delivered by the $1 \times 24$ fiber splitter to each gradiometer. Because the sensors were assembled by hand, some of the beam paths were better aligned than others and so required less pump/probe power to perform optimally. Gradiometers requiring more power were paired with higher-power splitter ports and those requiring less power were paired with lower-power ports. This left some gradiometers with less-than-ideal power which also led to a decrease in sensitivity.

### 3.2 Operation in a high-field environment

Another relevant test of sensor performance is its operating range. Many magnetic shields have residual magnetic fields and gradients present, which presents a problem for SERF magnetometers. The four on-board coils in each of our sensors are integral in compensating for excess fields to keep the atomic vapor operating in the SERF regime.

To test the DC dynamic range of the OPM sensors, one gradiometer was placed into a 4-layer mu-metal shield with one pair of Helmholtz coils along cylindrical shield can axis and two pairs of saddle coils in the transverse directions to control offset fields inside of the shield. (Fig. 6(a)). DC fields were applied to one of three large external offset coils embedded in the shield. The sensor then compensated for these fields with its on-board Helmholtz and saddle coils. In the sensitive direction ($z$-direction), a field offset of up to 80 nT was compensated for with the two on-sensor Helmholtz coils without noticeable degradation of the gradiometer performance. Current fluctuations in the offset coils caused global magnetic fluctuations which were common to both magnetometers and sub-

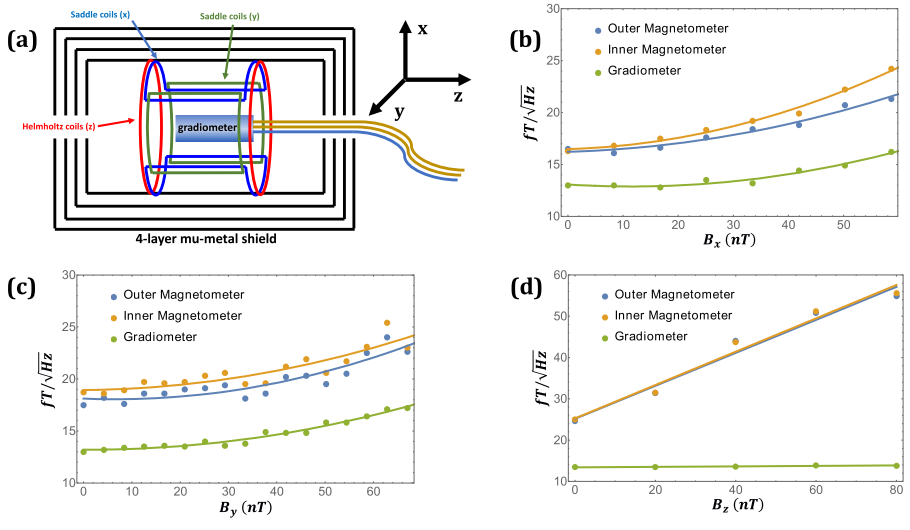


**Figure 6** (**a**) Diagram of setup to test sensor operating range. A gradiometer is placed in a 4-layer mu-metal shield with Helmholtz coils to provide magnetic field along cylindrical shield can axis and two saddle coils to provide field in the transverse directions. Helmholtz and saddle coils embedded in the sensor compensate for DC fields from the shield's coils. Sensitivity as a function of (**b**) the transverse field offset, parallel to pump/probe laser, (**c**) the transverse field offset, orthogonal to laser and sensitive direction, and (**d**) the field offset in sensitive direction

tracted in the gradiometer signal. Saddle coils shared between the two magnetometers making up the gradiometer compensated for the field offsets in the two transverse directions ($x$ and $y$). As the field was increased, the on-board saddle coils could not compensate for this field uniformly and so could not simultaneously null the field across the two vapor cells. At 70 nT transverse field, a degradation of the gradiometer sensitivity of 50% was measured. This is due mainly to the broadening of the magnetic resonance line as the high magnetic field transitions the atomic vapor out of the SERF regime. Independent control of the transverse fields across each magnetometer, for example, with independent saddle coil pairs around each cell, would reduce the inhomogeneity and improve performance at larger offset fields.

### 3.3 Closed-loop operation

The OPM sensors are operated in a closed feedback loop, where the internal field is continuously zeroed and the magnetometer outputs represent the coil-generated fields required to compensate the ambient fields. The two field readings (one per OPM in each sensor) are digitally subtracted to form the gradiometer output. Operating under negative feedback yields a better response linearity with increasing magnetic signal amplitude. In open-loop mode, by contrast, the atomic response becomes nonlinear at a few nanotesla as atoms are driven near the edges of the atomic resonance. In closed-loop mode, the lock-in output signal is fed back on the Helmholtz coils, keeping the atoms at zero field and in the center of the resonance.

To demonstrate the superiority of closed-loop operation, we placed one of our gradiometers in the same 4-layer mu-metal shield as in the previous section and applied a 30 Hz magnetic signal of various amplitudes via the shield's Helmholtz coils. In closed-loop mode, the relation between measured and actual magnetic signal amplitude remains linear (with a deviation from ideal linearity of <10%) even in the presence of signals >10 nT. In comparison, deviation of 10% from ideal linearity is surpassed already at a 5 nT signal field in open-loop mode (see Fig. 7). While the closed-loop operation increased the linearity, we still measure a significant degradation at larger signal fields. This region could be expanded further with more gain in the feedback loops.

Operation under negative feedback is a robust measurement technique which improves functionality in a non-ideally shielded environment. Scale factors for closed-loop OPMs are more stable than open-loop scale factors since they depend predominantly on the Helmholtz coil geometry. Closed-loop OPMs require a single calibration and magnetic

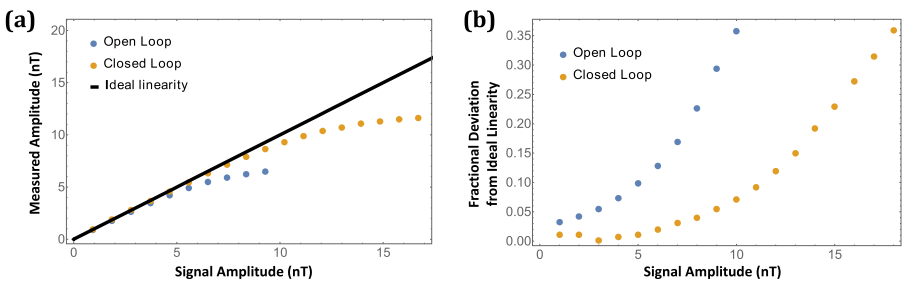


**Figure 7** Linearity of magnetometer response. (**a**) Magnetometer response in open-loop and closed-loop mode as field modulation amplitude increases. (**b**) Fractional deviation of open/closed loop magnetometers in (a) from the ideal linearity (black line)

field readings remain stable despite drifts in laser and cell parameters and the external magnetic field environment. This is due to the fact that, even though the lock-in signal slope changes (which impacts open-loop calibration factors), the zero-field point does not change. Thus, any external fields can be zeroed using the Helmholtz coils, whose calibration factor does not change.

In our closed-loop operation the bandwidth of the gradiometers is decreased from 230 Hz (in open-loop mode) to 150 Hz due to the increased latency of the electronics. We believe that this is not a fundamental issue but highlights a specific limitation of our electronics and feedback implementation. Because of the addition of transfer function poles introduced by the feedback, the latency increases. This can be remedied by additional zeros and poles designed specifically to increase bandwidth (i.e., decrease rise time in response to a unit step).

When operating under negative feedback, cross-talk between magnetometers becomes a larger concern. Increasing the density of magnetometers reduces the error in magnetic source localization for MEG. However, as the distance between magnetometers decreases, the modulating coils from one sensor start to influence the measurements of nearby sensors [27]. To address this problem in hardware, we have developed more sophisticated feedback coils than a simple Helmholtz geometry and have reduced the crosstalk from 8% to 0.8% at the closest possible sensor spacing of 1.25 cm and from 2% to 0.1% between the two magnetometers that constitute a gradiometer with 2 cm spacing [28]. This has not yet been implemented in this array but is a crucial next step in advancing OPM-based MEG technology.

## 4 Conclusion

We have developed a measurement system capable of supporting 24 gradiometers (48 magnetometers) and can perform high-sensitivity measurements for magnetoencephalography in a poorly-shielded and noisy environment. This is the first demonstration of a system designed for MEG based on OPMs to employ gradiometers arrayed radially, which allows for the rejection of systematic noise to a large degree. Despite a 10 GHz spread in cell resonance frequencies and considerable laser and mechanical noise, our gradiometers were able to consistently operate with noise floors below 25 $fT/Hz^{1/2}$ with a median of 15.4 $fT/Hz^{1/2}$ in a magnetic shield equipped for human trials.

We have shown that operating all magnetometers in closed-loop mode allows for a better signal linearity and increased dynamic range at the cost of bandwidth. Constant feedback also yields a measurement system that is more robust to ambient field drift and systematic changes that degrade calibration factors in open-loop operation.

These developments are especially important for researchers and technicians who do not have access to high-cost passively shielded rooms in which to acquire MEG images. The room-temperature nature of OPMs obviates any need for a liquid Helium dewar system and gives considerably more flexibility for sensor placement. Recent developments in coil design will also allow for denser magnetometer arrays and better current source localization in the brain as compared to state-of-the-art SQUID MEG systems.

**Acknowledgements**
We thank Dong Sheng for his initial work on the gradiometers, Branislav Korenko for lending his knowledge of electronics and help in assemble the electronics rack and human-sized shield. We also acknowledge Jeremy Hughes for his contributions in the design of the 3D-printed helmet and Shawn Geller for his help with the cell heating system.

**Funding**
This work was supported by the National Institute of Health under grants R01 EB019440, R01 NS094604, and R44NS090894.

**Abbreviations**
OPM, optically-pumped magnetometer; MEG, magnetoencephalography; SERF, spin-exchange relaxation-free; SQUID, superconducting quantum interference device; PCB, printed circuit board; PM, polarization-maintaining.

**Availability of data and materials**
The data generated and analyzed during the current study is available from the corresponding author on reasonable request.

**Competing interests**
The authors declare that they have no competing interests.

**Authors' contributions**
All authors participated in the development and assembly of the gradiometers. ARP characterized the microfabricated Rb cells as well as the individual magnetometers and gradiometers. NVN and SPK assembled the MEG system and characterized performance of simultaneously-running sensors in a human-sized shield. NVN developed the MEG software used to operate all gradiometers simultaneously and drafted the manuscript. SAK supervised the project. All authors read and approved the final manuscript.

## Publisher's Note


Received: 4 June 2020 Accepted: 31 August 2020 Published online: 11 September 2020

**References**
1. Cohen D. Magnetoencephalography: detection of the brain's electrical activity with a superconducting magnetometer. Science. 1972;175(4022):664–6.
2. O'Neill GC, Bauer M, Woolrich MW, Morris PG, Barnes GR, Brookes MJ. Dynamic recruitment of resting state sub-networks. NeuroImage. 2015;115:85–95.
3. Troebinger L, López JD, Lutti A, Bestmann S, Barnes G. Discrimination of cortical laminae using MEG. NeuroImage. 2014;102:885–93.
4. Vrba J, Anderson G, Betts J, Burbank MB, Cheung T, Cheyne D, Fife AA, Govorkov S, Habib F, Haid G, Haid V, Hoang T, Hunter C, Kubik PR, Lee S, McCubbin J, McKay J, McKenzie D, Nonis D, Paz J, Reichl E, Ressl D, Robinson SE, Schroyen C, Sekatchev I, Spear P, Taylor B, Tillotson M, Sutherling W. 151-channel whole-cortex MEG system for seated or supine positions. In: Recent advances in biomagnetism. 1999. p. 93–6.
5. Hämäläinen M, Hari R, Ilmoniemi RJ, Knuutila J, Lounasmaa OV. Magnetoencephalography—theory, instrumentation, and applications to noninvasive studies of the working human brain. Rev Mod Phys. 1993;65(2):413–97.
6. Rias B, Pfeiffer C, Schneiderman JF. Evaluation of realistic layouts for next generation on-scalp MEG: spatial information density maps. Sci Rep. 2017;7(1):6974.
7. Boto E, Bowtell R, Krüger P, Fromhold TM, Morris PG, Meyer SS, Barnes GR, Brookes MJ. On the potential of a new generation of magnetometers for MEG: a beamformer simulation study. PLoS ONE. 2016;11(8):e0157655.
8. Luessi M, Nummenmaa A, Lew S, Okada Y, Hämäläinen M. Performance evaluation of a novel pediatric MEG system. In: The 19th international conference of biomagnetism. Halifax, Canada. 2014.
9. Iivanainen J, Stenroos M, Parkkonen L. Measuring MEG closer to the brain: performance of on-scalp sensor arrays. NeuroImage. 2017;147:542–53.
10. Happer W, Tang H. Spin-exchange shift and narrowing of magnetic resonance lines in optically pumped alkali vapors. Phys Rev Lett. 1973;31:273.
11. Allred JC, Lyman RN, Kornack TW, Romaliz MV. High-sensitivity atomic magnetometer unaffected by spin-exchange relaxation. Phys Rev Lett. 2002;89(13):0801.
12. Sheng D, Perry A, Krzyzewski S, Geller S, Kitching J, Knappe S. A microfabricated optically-pumped magnetic gradiometer. Appl Phys Lett. 2017;110(3):031106.
13. Alem O, Mhaskar R, Jiménez-Martínez R, Sheng D, LeBlanc J, Trahms L, Sander T, Kitching J, Knappe S. Magnetic field imaging with microfabricated optically-pumped magnetometers. Opt Express. 2017;25(7):7849.
14. Knappe S, Alem O, Sheng D, Kitching J. Microfabricated optically-pumped magnetometers for biomagnetic applications. J Phys. 2016;723:012055.
15. Mhaskar R, Knappe SA, Kitching J. A low-power, high-sensitivity micromachined optical magnetometer. Appl Phys Lett. 2012;101(24):241105.
16. Borna A, Carter TR, Goldberg JD, Colombo AP, Jau Y-Y, Berry C, McKay J, Stephen J, Weisend M, Schwindt PDD. A 20-channel magnetoencephalography system based on optically pumped magnetometers. Phys Med Biol. 2017;62(23):8909–23.
17. Borna A, Carter TR, Colombo AP, Jau Y, McKay J, Weisend M, Taulu S, Stephen JM, Schwindt PDD. Non-invasive functional-brain-imaging with an OPM-based magnetoencephalography system. PLoS ONE. 2020;15(1):e0227684.
18. Boto E, Holmes N, Leggett J, Roberts G, Shah V, Meyer SS, Muñoz LD, Mullinger KJ, Tierney TM, Bestmann S, Barnes GR, Bowtell R, Brookes MJ. Moving magnetoencephalography towards real-world applications with a wearable system. Nature. 2018;555:657–61.
19. Tierney TM, Holmes N, Meyer SS, Boto E, Roberts G, Leggett J, Buck S, Duque-Muñoz L, Litvak V, Bestmann S, Baldeweg T, Bowtell R, Brookes MJ, Barnes GR. Cognitive neuroscience using wearable magnetometer arrays: non-invasive assessment of language function. NeuroImage. 2018;181:513–20.

20. Johnson CN, Schwindt PDD, Weisend M. Multi-sensor magnetoencephalography with atomic magnetometers. Phys Med Biol. 2013;58(17):6065–77.
21. Lee HJ, Shim JH, Moon HS, Kim K. Flat-response spin-exchange relaxation free atomic magnetometer under negative feedback. Opt Express. 2014;22(17):19887–94.
22. Preusser J, Knappe SA, Gerginov V, Kitching J. A microfabricated photonic magnetometer. In: European conference on lasers and electro-optics and the European quantum electronics conference. Munich, Germany. 2009.
23. Mescher MJ, Lutwak R, Varghese M. An ultra-low-power physics package for a chip-scale atomic clock. In: The 13th international conference on solid-state sensors, actuators and microsystems, 2005. Digest of technical papers. TRANSDUCERS'05. Seoul, South Korea. 2005.
24. [Online]. Available. www.toptica.com.
25. [Online]. Available. www.quspin.com.
26. Krzyzewski SP, Perry AR, Gerginov, V, Knappe SA. Characterization of noise sources in a microfabricated single-beam zero-field optically-pumped magnetometer. J Appl Phys. 2019;126(4):044504.
27. ter Brake HJM, Fleuren FH, Ulfman JA, Flokstra J. Elimination of flux-transformer crosstalk in multichannel SQUID magnetometers. Cryogenics. 1986;26(12):667–70.
28. Nardelli NV, Krzyzewski SP, Knappe SA. Reducing crosstalk in optically-pumped magnetometer arrays. Phys Med Biol. 2019;64(21):21NT03.